

The deconvolution of lunar brightness temperature based on the maximum entropy method using Chang'e-2 microwave data *

Shu-Guo Xing, Yan Su, Jian-Qing Feng and Chun-Lai Li

National Astronomical Observatories, Chinese Academy of Sciences, Beijing 100012, China;
suyan@nao.cas.cn

Received 2013 November 11; accepted 2014 June 1

Abstract A passive and multi-channel microwave sounder onboard the Chang'e-2 orbiter has successfully acquired microwave observations of the lunar surface and subsurface structure. Compared with the Chang'e-1 orbiter, the Chang'e-2 orbiter obtained more accurate and comprehensive microwave brightness temperature data, which are helpful for further research. Since there is a close relationship between microwave brightness temperature data and some related properties of the lunar regolith, such as the thickness, temperature and dielectric constant, precise and high resolution brightness temperature data are necessary for such research. However, through the detection mechanism of the microwave sounder, the brightness temperature data acquired from the microwave sounder are weighted by the antenna radiation pattern, so the data are the convolution of the antenna radiation pattern with the lunar brightness temperature. In order to obtain the real lunar brightness temperature, a deconvolution method is needed. The aim of this paper is to solve the problem associated with performing deconvolution of the lunar brightness temperature. In this study, we introduce the maximum entropy method (MEM) to process the brightness temperature data and achieve excellent results. The paper mainly includes the following aspects: first, we introduce the principle of the MEM; second, through a series of simulations, the MEM has been verified as an efficient deconvolution method; and third, the MEM is used to process the Chang'e-2 microwave data and the results are significant.

Key words: space vehicles — instruments: microwave sounder — Moon: brightness temperature — methods: maximum entropy method

1 INTRODUCTION

The Chang'e-2 orbiter was launched on 2010 October 1. The microwave sounder was one of the main payloads on both Chang'e-1 and Chang'e-2 orbiters, which was passive and had four channels (3 GHz, 7.8 GHz, 19.35 GHz, 37 GHz) (Jiang et al. 2010). During on-orbit observation, both microwave sounders obtained a large amount of microwave radiation brightness temperature data. Extensive research has been carried out using these microwave brightness temperature data (Fa & Jin 2010; Wang et al. 2010). Benefiting from the lower orbital altitude, the spatial resolution of

* Supported by the National Natural Science Foundation of China.

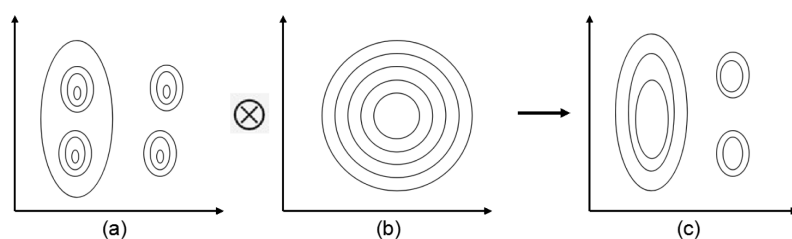


Fig. 1 The diagram of the impact of the antenna pattern. (a) The original map; (b) the antenna pattern; and (c) the observation map (the convolution of (a) and (b)).

the microwave sounder on the Chang'e-2 orbiter is nearly twice as high as that of Chang'e-1. In addition, Chang'e-2 measurements covered the lunar surface more completely and collected more tracks of swath data than Chang'e-1. Therefore, more available data can be used to research the radiation characteristics of the lunar surface and subsurface structure. In this paper, we choose the 37 GHz microwave data, which better reflect the lunar surface microwave radiation. Moreover, the Laser Altimeter and the Charge Coupled Device (CCD) camera are also the main payloads on the Chang'e-2 orbiter, thus the Digital Elevation Model (DEM) and CCD images are direct responses to lunar surface structure. Hence, we use the DEM and CCD images to verify the results of the deconvolution.

It is known that in the detection mechanism of the microwave sounder, antenna brightness temperature has been weighted by the antenna radiation pattern. It is the convolution of the antenna radiation pattern and the lunar brightness temperature. The result of this impact is shown in Figure 1. Because of the impact of the antenna pattern, points close together on the original map (Fig. 1(a)) cannot be distinguished in the observation map (Fig. 1(c)). Actually, when using the brightness temperature data for research, we suppose the lunar brightness temperature is approximately equal to the antenna brightness temperature, but this will cause a loss of details and a decrease in spatial resolution (Feng et al. 2013). The paper introduces a deconvolution method, named the maximum entropy method (MEM), to eliminate the influence of the antenna pattern. In the field of image reconstruction of radio astronomy, the MEM is a valuable tool that has many advantages in dealing with both extended sources and point sources (Starck et al. 2002).

This paper is organized as follows. In Section 2, a brief description on the principle of MEM is given. In Section 3, a series of simulations is carried out to verify the validity of the MEM. In this section, we introduce two indices, the Mean Squared Error (MSE) and the Peak Signal to Noise Ratio (PSNR), to evaluate the quality of the deconvolution. Through the simulations, we come to the conclusion that the MEM is an efficient deconvolution method. In Section 4, the MEM is used to process the Chang'e-2 brightness temperature data. A new brightness distribution map is shown and compared with the original map, and we also choose several local regions for discussions of the results. Finally, the conclusion of this work is stated in Section 6.

2 THE PRINCIPLE OF THE MEM

In the field of image restoration, Frieden first introduced the concept of image entropy in 1972 (Frieden 1972) and gave the expression, $S = -\sum x(i, j) \ln x(i, j)$, where x defined the gray value of the image at points i and j . With the introduction of image entropy, a new constraint condition was applied in the field of image restoration. Based on the different background and limitations in the application of the MEM, Frieden, Gull and Bryan proposed different MEMs named by the authors names respectively (Frieden 1972; Gull & Daniell 1978; Skilling & Bryan 1984). The MEM used in this paper is based on the method proposed by Bonavito et al. (1993).

Here, the model used in the paper is shown as below

$$\begin{cases} \text{subject to } y(i, j) = x(i, j) \otimes \text{PSF}, \\ \text{max } S = - \sum x(i, j) \cdot \ln x(i, j), \\ \text{find } x(i, j). \end{cases}$$

In the above model, x means the original map, y means the observed map, PSF means the antenna pattern and the model indicates that the best solution of the deconvolution needs to obey the constraint of maximum entropy.

With the Lagrange multiplier method, we obtain the maximum entropy distribution,

$$x(i, j) = \exp\left(- \sum_{m,n=1,1}^{i,j} \lambda mn \cdot \text{PSF}\right) / Z(\lambda_{11}, \dots, \lambda_{ij}), \tag{1}$$

$$Z(\lambda_{11}, \dots, \lambda_{ij}) = \sum_{1,1}^{i,j} \exp\left(- \sum_{m,n=1,1}^{i,j} \lambda mn \cdot \text{PSF}\right), \tag{2}$$

where Z means the partition function and λ means Lagrange multipliers. Also, a parameter is defined as

$$G = x(i, j) \otimes \text{PSF} - y(i, j). \tag{3}$$

Here we use a more storage-efficient method of successive approximation. Our recursion relation is defined as

$$\lambda(\text{New}) = \lambda(\text{old}) - \ln\left(\frac{y}{y - G}\right). \tag{4}$$

The steps are as follows: in the first step, we set all $\lambda = 0$; in the second step, with the $\lambda = 0$, we find an original value for x from Equation (1); in the third step, we put x , PSF and y in Equation (3), and we calculate G ; and in the fourth step, having the value of G , we calculate the new value of λ from Equation (4). Then based on the new λ , we repeat the second step through fourth steps, until λ converges. This method starts with $\lambda = 0$, which corresponds to a scene that is a flat map (a map with the maximum possible entropy). The entropy of the scene decreases with each iteration as it converges to the scene with the maximum entropy that satisfies the constraints of the original map and the PSF. For more details, please refer to Bonavito et al. (1993).

3 THE SIMULATION AND VERIFICATION

The simulation includes three aspects, namely the simulation based on a point source, the simulation based on an extended source and the simulation based on the Chang'e-2 microwave brightness temperature data, respectively. Two indices, the MSE and the PSNR, are used to evaluate the quality of the deconvolution. A lower MSE and a higher PSNR indicate better deconvolution results. The definitions of the MSE and PSNR are given below.

$$\text{MSE} = \frac{1}{mn} \sum_{i=0}^{m-1} \sum_{j=0}^{n-1} [Y(i, j) - X(i, j)]^2, \tag{5}$$

$$\text{PSNR} = 10 \cdot \log_{10}\left(\frac{\text{MAX}^2}{\text{MSE}}\right), \tag{6}$$

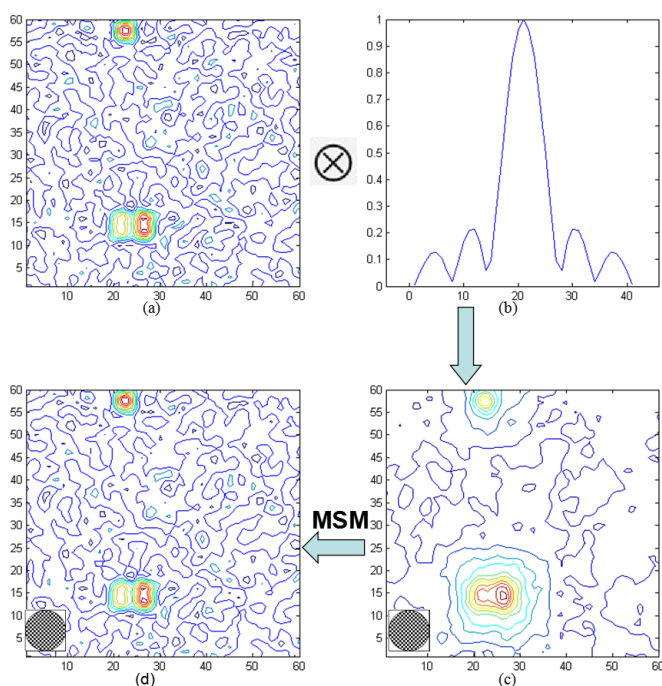


Fig. 2 A schematic representation of the simulation process based on point sources: (a) the original map; (b) the antenna pattern; (c) the blurred map; and (d) the deconvolved map.

where X means the original map, Y means the map to be evaluated and MAX means the maximum value of data representing X . Here, the pattern function used to fit the antenna pattern is shown as below,

$$f(\theta) = \text{sin c} \left(\frac{D * \sin(\theta)}{\lambda} \right), \quad (7)$$

where D is the diameter of the ground antenna, λ is the observation wavelength and θ is the antenna pattern angle. The function is used in Section 3.1 and Section 3.2 .

3.1 Simulation Based on Point Sources

The purpose of the simulation is to verify the validity of the method when dealing with a point source. The steps of the simulation are as follows.

First, in Figure 2(a), the original data contain three point sources and the values of the point sources are higher than the background. The second step is fitting an antenna pattern using Equation (7). Figure 2(b) shows a two-dimensional curve of the antenna pattern. The third step is convolving the original data with the antenna pattern, then the blurred map is shown in Figure 2(c). The fourth step is using the MEM to process the blurred map, and the result of the deconvolution is shown in Figure 2(d). In addition, the shadows on the lower left of Figure 2(c) and Figure 2(d) represent the projection of 3 dB beam width on the original map and the deconvolved map, respectively.

Because of the impact of the beam width from the antenna pattern, the two point sources in the bottom part of Figure 2(c) nearly become indistinguishable. However, after deconvolution using the MSE is applied, those two point sources can be clearly identified in Figure 2(d). Compared with the blurred map, the deconvolved map based the MEM recovers the details found in the original data

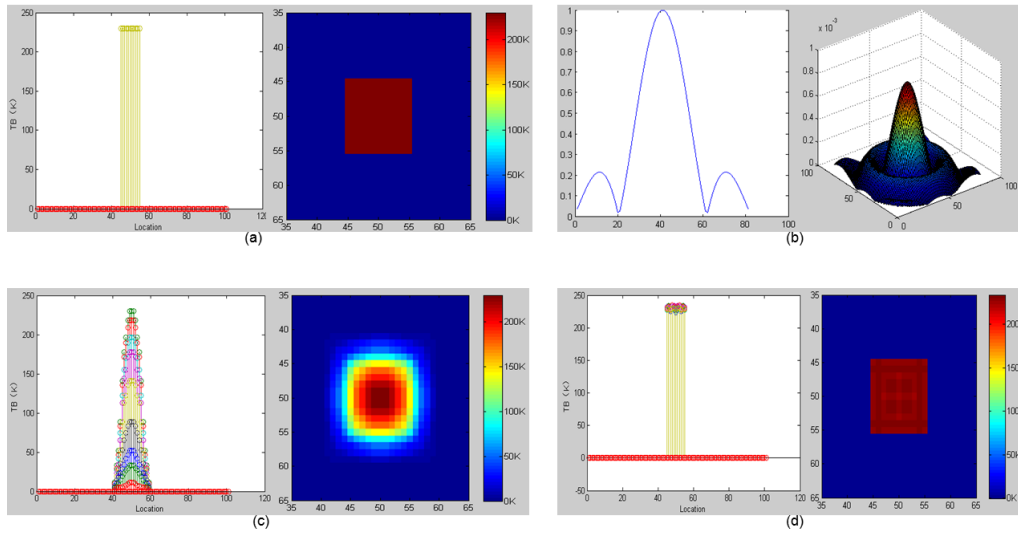


Fig. 3 The simulation based on the ground antenna. (a) The original source; (b) the antenna pattern; (c) the blurred map; and (d) the deconvolved map.

map. Moreover, we can calculate the MSE and PSNR. The MSE and PSNR of the deconvolved map are 0.0113 and 58.3980 respectively, while the values are 0.6309 and 40.9298 for the blurred map. This result demonstrates that the process of deconvolution improves the PSNR and reduces the MSE.

3.2 Simulation Based on An Extended Source

In this simulation, first, an original extended source is shown in Figure 3(a). The value in the middle area is 230 K, while the value in other areas is 0 K. Two forms, the discrete sequence image and the plane image, are shown in order to clearly illustrate the changes between the different images. Second, based on Equation (7), the antenna pattern is shown in Figure 3(b). Then, by convolving the original data with the antenna pattern, the blurred image is shown in Figure 3(c). Finally, using the MEM to process the blurred image, the result of the deconvolution process is shown in Figure 3(d).

We calculate the MSE and PSNR. The MSE and PSNR of the blurred map are 0.6608 and 40.1589 respectively, while the values are 0.0466 and 51.6718 in the deconvolved map. Figure 4 shows the residual map of the blurred map and the deconvolved map. The range of values in the residual map of the blurred map is from -150 K to 100 K but the range of values is from about -0.13 K to 0.17 K in the deconvolved map. Hence, when processing the extended source data, the MEM produced a better result.

3.3 Simulation Based on Chang'e-2 Microwave Data

During the ground calibration testing, we tested the antenna pattern and gain of the 37 GHz channel and obtained four important parameters: (1) the 3 dB beam width that is approximately 10° ; (2) the main beam width that is about 26° ; (3) the attenuation of the first side lobe is about 22 dB; and (4) the beam width of the first side lobe that is approximately 6° . Based on a Gaussian function, we fitted the antenna pattern function using the above four parameters (the contribution of the main lobe

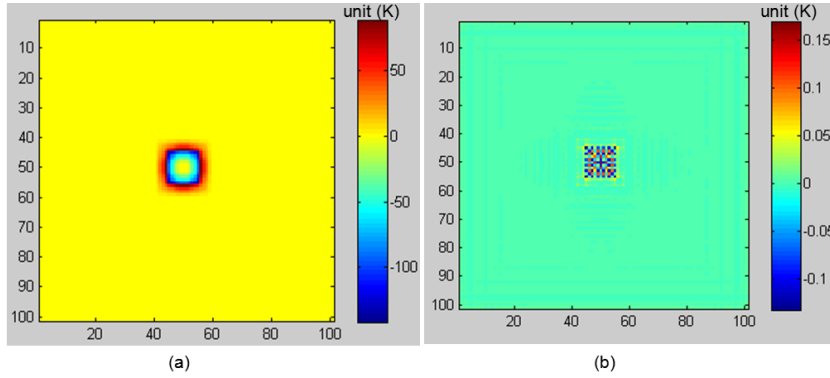


Fig. 4 The residual map of the blurred map and the maximum entropy map. (a) The blurred one; (b) the deconvolved one. The maps are obtained from the blurred map and the deconvolved map minus the corresponding original map.

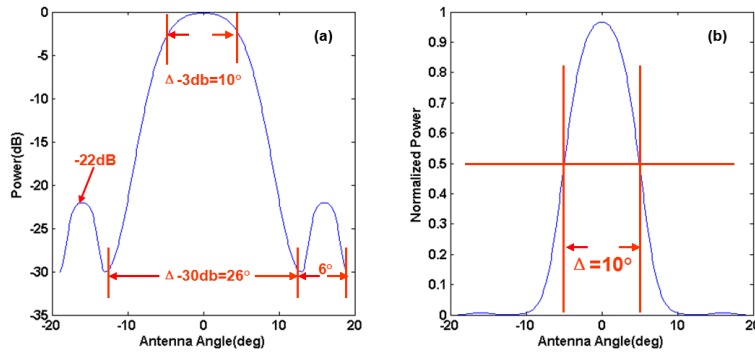


Fig. 5 The antenna pattern of 37 GHz, (a) the gain (dB) antenna pattern, and (b) the normalized antenna pattern. According to Wang et al. (2009), the antenna pattern of 37 GHz is derived and used in the following deconvolution processing procedure.

is about 95.9% (Wang et al. 2009), so here we only consider the main lobe and the first side lobe, which are shown in Equation (8). The antenna pattern is shown in Figure 5.

In addition, considering that the bandwidth of the 37 GHz channel is about 500 MHz, we tested the antenna pattern and gain at three frequency points (36.47, 37, 37.53 GHz) during ground calibration testing. Taking the 3 dB beam width for instance, the three frequency points (36.47, 37, 37.53 GHz) corresponded to 10.07° , 10.17° and 10.03° respectively. The difference is less than 0.15° , which is about 0.25 km on the lunar surface. However, the spatial resolution of the 37 GHz channel is 13 km, far larger than 0.25 km. So in this paper, we only use the antenna pattern corresponding to 37 GHz to represent the whole bandwidth.

$$f(\theta) = \begin{cases} -30 \cdot e^{-\left(\frac{\theta+13}{5.3}\right)^2} - 30 \cdot e^{-\left(\frac{\theta-13}{5.3}\right)^2}, & -13^\circ \leq \theta \leq 13^\circ, \\ -8 \cdot e^{-\left(\frac{|\theta|-13}{5.3}\right)^2} - 8 \cdot e^{-\left(\frac{|\theta|-13}{0.23}-26\right)^2} - 22, & 13^\circ \leq |\theta| \leq 19^\circ. \end{cases} \quad (8)$$

In this simulation, the Chang'e-2 microwave data are used as the original data. The purpose of the simulation is to verify that the method used in this step can work well when processing the

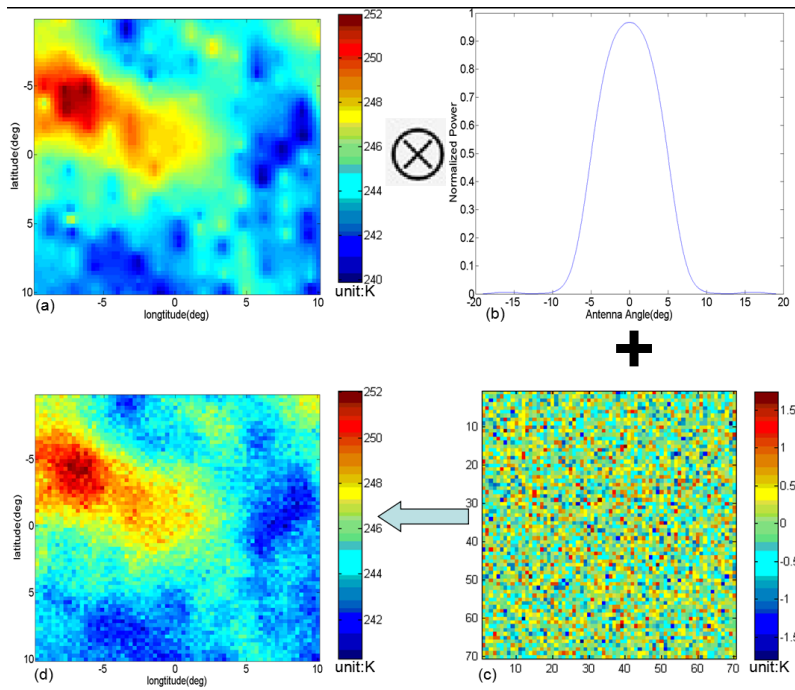


Fig. 6 The result of a simulation based on the Chang’e-2 microwave data. (a) The original brightness temperature map; (b) the antenna pattern; (c) the Gaussian noise; and (d) the blurred map.

Chang’e-2 microwave data with the corresponding antenna pattern. Firstly, a region about $20^\circ \times 20^\circ$, chosen from the Chang’e-2 microwave brightness temperature map, is shown in Figure 6(a). Since we choose the 37 GHz microwave data, the corresponding beam width of the antenna pattern is about 10° (Wang et al. 2009); the antenna pattern map is shown in Figure 6(b). Given that the sensitivity of the Chang’e-2 microwave sounder is approximately 0.5 K (Wang et al. 2009), a Gaussian noise map is shown in Figure 6(c), whose mean and standard deviation are 0 and 0.5 respectively. Figure 6(d) shows the blurred map, which is obtained by convolving the original map with the antenna pattern and then adding noise.

Here, different methods, such as the Richardson-Lucy (R-L) deconvolution method and the blind deconvolution method (Ayers & Dainty 1988; Biggs & Andrews 1997) are chosen to process the same data, and we compare the processing results. The comparison is shown in Figure 7. We also calculate the MSE and PSNR of the different methods, which are shown in Table 1. By comparison, we find that the MEM shows a significant advantage both in terms of restoring the details and restraining the noise.

Table 1 The PSNR and MSE of the Different Methods

	Blurred	MEM	Blind method	R-L method
PSNR	52.8063	57.8611	50.4692	52.7997
MSE	0.3404	0.1039	1.2300	0.3333

Notes: The PSNR and MSE are calculated referring to Eqs. (5) and (6).

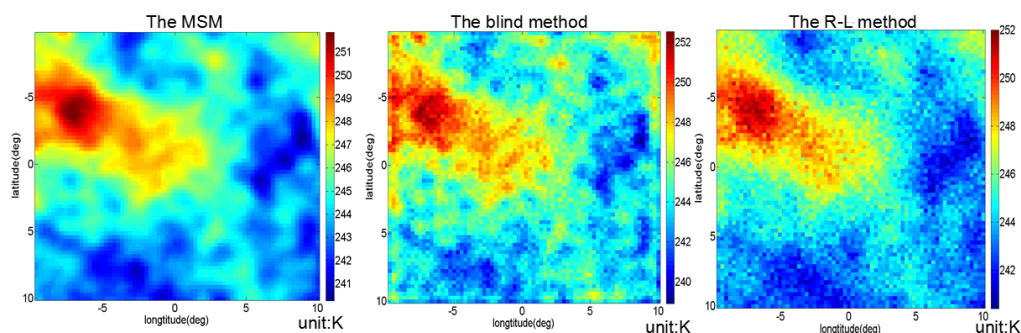


Fig. 7 The deconvolution results from different methods.

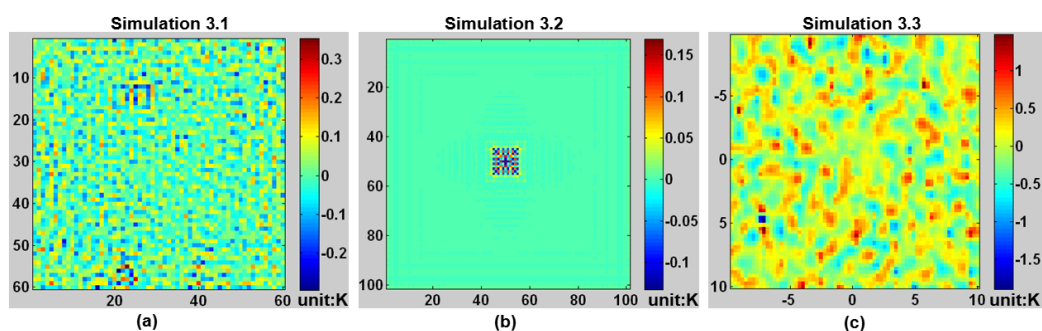


Fig. 8 Error produced in the above three simulations. (a) Simulation based on point sources; (b) simulation based on an extended source; and (c) simulation based on the real microwave data.

3.4 Error Analysis

Through the above three simulations, we found that the MEM is a good method to solve the deconvolution problem. In this section, we discuss the radiometric error introduced by the MEM.

Figure 8 shows the error produced in the above three simulations, which is found by the deconvolved map minus the corresponding original map. We found that in simulation 1, the range of error is from -0.35 K to 0.4 K with a standard deviation $\sigma = 0.0676$ K; in simulation 2, the error is from -0.13 K to 0.17 K with $\sigma = 0.0089$ K; and in simulation 3, because of the Gaussian noise (-1.8 K to 1.8 K) introduced, the error is from about -2 K to 1.5 K with $\sigma = 0.3054$ K. The errors introduced by the MEM in the above three simulations are all less than the sensitivity of the microwave sounder, which is 0.5 K (Wang et al. 2009).

Through the above simulations and error analysis, we can draw the conclusion that the MEM is an efficient method when dealing with the deconvolution problem and it can further be used to process the microwave brightness temperature data acquired by the Chang'e-2 orbiter.

4 DATA PROCESSING BASED ON CHANG'E-2 MICROWAVE DATA

In this section, the MEM is used to process the real microwave data. The data are the 37 GHz nighttime microwave data acquired by the Chang'e-2 orbiter, which are normalized by the lunar local time. Referring to Zheng et al. (2012), we normalize the lunar hour angle to 0° , which implies

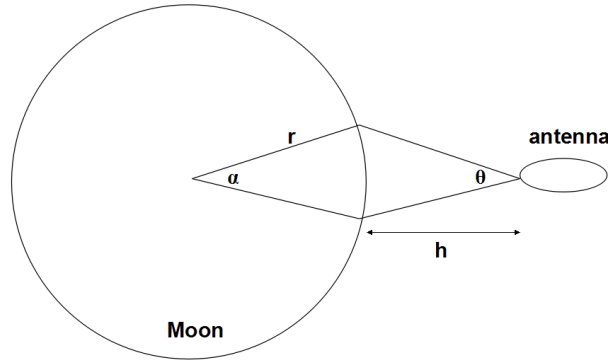


Fig. 9 A schematic diagram of the antenna observation.

the lunar time is the midday of the Moon. There is also a problem worthy of notice, which is how to keep the scale of the microwave data consistent with the antenna pattern. Figure 9 clearly illustrates this problem.

In Figure 9, h means the observation height of the antenna, θ means the angle of the antenna pattern, r means the radius of the Moon and α means the central angle of the Moon. In order to maintain a consistent projection of θ and α on the lunar surface, we derive an approximate equation, shown in Equation (9). With further simplification, we get $\theta \approx 17.4\alpha$, which means that 1° on the lunar surface corresponds to 17.4° in the antenna angle. When the microwave data value is taken every 0.2° , the corresponding antenna pattern value is taken every 3.48° . Thus, the correspondence of 0.2° in the microwave data with 3.48° in the antenna pattern is adopted in this paper.

$$\frac{\alpha}{180} \times \pi \times r \approx \frac{\theta}{180} \times \pi \times h. \quad (9)$$

In addition, the DEM data and the CCD data from the Chang'e-2 orbiter are used in this section. The laser altimeter and the CCD camera are also the main payloads on the Chang'e-2 orbiter and the spatial resolution of the two payloads is higher than that of the microwave sounder. So, the data are used to verify the validity of the newly added details in the deconvolved map. A comparison of the original distribution map and the deconvolved distribution map based on the MEM is shown in Figure 10.

Furthermore, three regions are also chosen to show the differences between the original map and the deconvolved map. The range of the first region is from 14.3°W to 11.27°E and 48.2°S to 22.4°S . The second region is about $10^\circ \times 10^\circ$ and centered at the Apollo 16 landing point, while the third region is centered at the Luna 24 landing point. Comparisons of the three regions are shown in Figures 11, 12 and 13 respectively.

Figure 10 indicates that the deconvolved map of brightness temperature has a higher resolution than the original map. In order to clearly compare the deconvolved map with the the original map, we chose three regions. From Figures 11, 12 and 13, we find that there are some newly added details which are bounded by blue lines in the deconvolved map. Furthermore, in corresponding positions, we find similar features in both the DEM and the CCD maps.

In deconvolved maps, under the conditions of only considering the influence of the antenna pattern, the error in brightness temperature introduced by the MEM is less than 0.5 K.

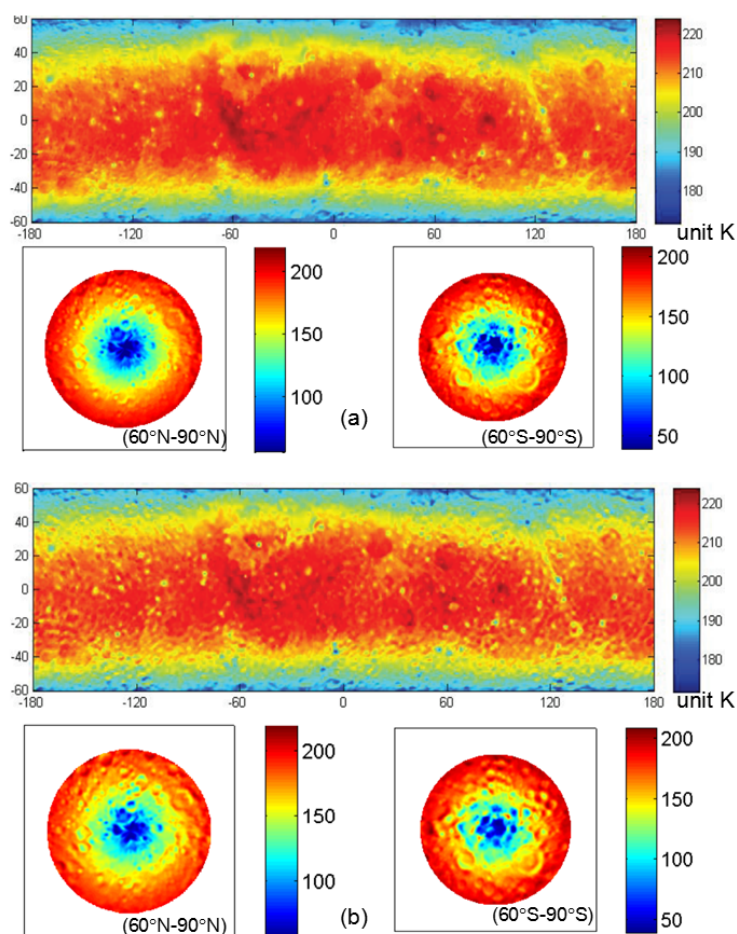


Fig. 10 A comparison of the original map and the deconvolved map of the whole lunar surface, (a) the original map, and (b) the deconvolved map. The original data came from the 37 GHz nighttime microwave data.

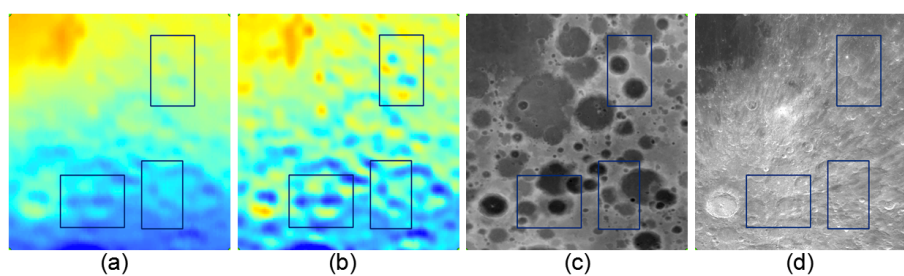


Fig. 11 A map to show comparisons of the same region. The region has a range of longitude from 14.3°W to 11.27°E and a range of latitude from 48.2°S to 22.4°S . (a) the original brightness temperature map, (b) the deconvolved brightness temperature map, (c) the DEM map, and (d) the CCD map.

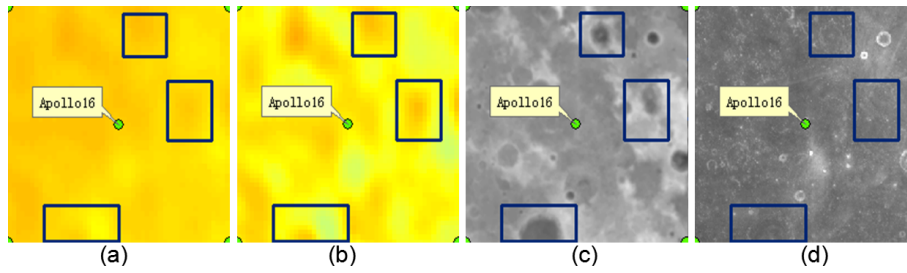


Fig. 12 A map to show comparisons of the same region. The region has a range of longitude from 57.2°E to 67.2°E and a range of latitude from 7.3°N to 17.3°N . (a) The original brightness temperature map, (b) the deconvolved brightness temperature map, (c) the DEM map, and (d) the CCD map.

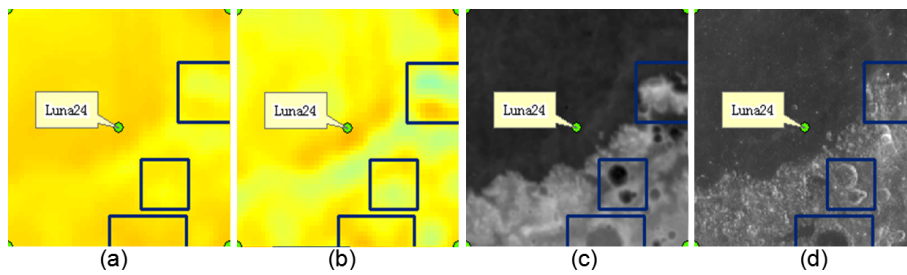


Fig. 13 A map to show comparisons of the same region. The region has a range of longitude from 10.5°E to 20.5°E and a range of latitude from 14°S to 4°S . (a) The original brightness temperature map, (b) the deconvolved brightness temperature map, (c) the DEM map, and (d) the CCD map.

5 CONCLUSIONS

In this paper, the MEM is first used to deconvolve the Chang'e-2 microwave data and the results are satisfactory. Compared to the original brightness temperature map, the map processed by the MEM has more details and a higher resolution. Only considering the influence of the antenna pattern, the new data obtained by MEM processing are very useful for further research. In addition, the error in brightness temperature introduced by the MEM is less than 0.5 K. We conclude the following.

Given the impact of the antenna pattern, it is necessary to find a suitable deconvolution method used to process the Chang'e-2 microwave data. By applying the simulations above, on the one hand, we found the impact of the antenna pattern could heavily blur the original map, but on the other hand, the MEM was effective in increasing PSNR and reducing MSE, for both extended sources and point sources, eventually restoring information about the original distribution. Furthermore, compared to other methods, the MEM shows significant advantages, both for restoring detail and reducing noise.

After making comparisons of the whole lunar brightness temperature distribution map and several local regions, we found the deconvolved maps had more details and a higher resolution than the original maps. These results indicate that a more precise and higher resolution brightness temperature map has been produced.

By comparing the brightness temperature map with the topographic map, we found the newly added details also have a correspondence with the CCD map and DEM map. This, for one thing, verifies the validity of the newly added details, and also reveals a relation between the brightness

temperature and the lunar terrain and geological formations. Thus, the precise brightness temperature data processed by the MEM are very useful for studying the lunar surface and subsurface structure in further research.

Acknowledgements This work is supported by the National Natural Science Foundation of China (Grant Nos. 11173038 and 11203046). We thank the Lunar and Deep Space Exploration Department, National Astronomical Observatories, Chinese Academy of Sciences (NAOC) for providing the microwave data, as well as CCD and DEM maps.

References

- Ayers, G. R., & Dainty, J. C. 1988, *Optics Letters*, 13, 547
- Biggs, D. S. C., & Andrews, M. 1997, *Appl. Opt.*, 36, 1766
- Bonavito, N. L., Dorband, J. E., & Busse, T. 1993, *Appl. Opt.*, 32, 5768
- Fa, W., & Jin, Y.-Q. 2010, *Icarus*, 207, 605
- Feng, J.-Q., Su, Y., Liu, J.-J., Zou, Y.-L., & Li, C.-L. 2013, *RAA (Research in Astronomy and Astrophysics)*, 13, 359
- Frieden, B. R. 1972, *Journal of the Optical Society of America (1917–1983)*, 62, 511
- Gull, S. F., & Daniell, G. J. 1978, *Nature*, 272, 686
- Jiang, J.-S., Wang, Z., Zhang, X., et al. 2010, in *Geoscience and Remote Sensing Symposium (IGARSS), 2010 IEEE International*, 4282
- Skilling, J., & Bryan, R. K. 1984, *MNRAS*, 211, 111
- Starck, J. L., Pantin, E., & Murtagh, F. 2002, *PASP*, 114, 1051
- Wang, Z.-Z., Li, Y., Jiang, J., & Li, D. 2010, *Science China Earth Sciences*, 53, 1365
- Wang, Z.-Z., Li, Y., Zhang, X., Jiang, J., et al. 2009, *Sci China Ser D-Earth Sci*, 39, 1029 (in Chinese)
- Zheng, Y. C., Tsang, K. T., Chan, K. L., et al. 2012, *Icarus*, 219, 194